

# ABAQUS implementation of cohesive zone models

Emilio Martínez-Pañeda<sup>a,\*</sup>

<sup>a</sup>*Department of Mechanical Engineering, Technical University of Denmark, DK-2800  
Kgs. Lyngby, Denmark*

---

## Abstract

Documentation that accompanies the file UEL3.f - a user element subroutine (UEL) with a general implementation of cohesive zone models. If using this code for research or industrial purposes, please cite:

S. del Busto, C. Betegón, E. Martínez-Pañeda. A cohesive zone framework for environmentally assisted fatigue. *Engineering Fracture Mechanics* 185, pp. 210-226 (2017)

*Keywords:*

Cohesive zone models, Finite element analysis, ABAQUS, Fracture, Fatigue crack growth

---

## 1. Introduction

Cohesive zone models are a very popular computational tool to model fracture in engineering materials. The concept is simple: a cohesive force exists ahead of the crack that prevents the crack from propagating; this can be seen as a traction-separation law for the decohesion of atomic lattices. Material degradation and separation are thus assumed to take place in a discrete plane, represented by cohesive elements that are embedded in potential crack propagation paths. The micromechanisms of material degradation and failure are thus embedded into the constitutive law that relates the cohesive traction with the local separation.

---

\*Corresponding author. Tel: +45 45 25 42 71; fax: +45 25 19 61.  
*Email address:* mail@empaneda.com (Emilio Martínez-Pañeda)

The present code, employed for the first time in (del Busto et al., 2017), enables the modeling of crack initiation and growth under both monotonic and cyclic loading conditions. The code is distributed as a user element (UEL) subroutine for Abaqus under a BSD license (see accompanying text file). The present document accompanies the subroutine file and provides details about the (i) the constitutive traction-separation law (Section 2), (ii) the numerical implementation in the context of the finite element method (Section 3), and (iii) the very simple instructions required to run ABAQUS with the aforementioned subroutine (Section 4).

## 2. Cohesive zone formulation

Cohesive zone models are based on the pioneering works of Dugdale (1960) and Barenblatt (1962). The central point of all cohesive zone models is the function that describes the interaction force between the two interfaces (crack faces) (Kuna, 2013). This law represents a local material property that is independent of the external load. The so-called cohesive law or traction-separation law is usually a relation between the boundary tractions  $\sigma$  and the separation  $\delta = u_n^+ - u_n^-$  of the interfaces, i. e. the distance between the crack faces. Initially, the stress increases with growing distance up to a maximum, which is called the cohesive strength  $\sigma_{max}$  of the material. If the separation has reached a critical decohesion length  $\delta_c$ , then the material is completely separated and no stress can be transmitted. Integrating the separation law up to failure  $\delta_c$  yields the area under the curve that corresponds to the dissipated work during a materials separation - the specific fracture energy per surface area  $G_c = 2\gamma$  as introduced by Griffith,

$$G_c = \int_0^{\delta_c} \sigma(\delta) d\delta \quad (1)$$

i.e., the energy of separation. A wide range of traction-separation laws have been proposed, and their ability to properly deal with mixed-mode conditions is not exempt of controversy (McGarry et al., 2014; Park and Paulino, 2013). We here adopt Xu and Needleman (1993) cohesive law, one of the most popular traction-separation laws for metals. Other constitutive cohesive relations can be very easily incorporated into the code.

### 2.1. Xu-Needleman cohesive law

In (Xu and Needleman, 1993) a cohesive surface is defined ahead of the crack whose properties are characterized by relations between the normal

( $T_n$ ) and tangential ( $T_t$ ) tractions across this surface and the corresponding displacement jumps ( $\Delta_n$  and  $\Delta_t$ , respectively). This relations are derived from a potential  $\phi$  as

$$\mathbf{T} = -\frac{\partial\phi}{\partial\Delta} \quad (2)$$

with,

$$\begin{aligned} \phi = & \phi_n + \phi_n \exp\left(-\frac{\Delta_n}{\delta_n}\right) \left\{ \left[1 - r + \frac{\Delta_n}{\delta_n}\right] \frac{1-q}{r-1} - \right. \\ & \left. \left[ q + \frac{(r-q)}{(r-1)} \frac{\Delta_n}{\delta_n} \right] \exp\left(-\frac{\Delta_t^2}{\delta_t^2}\right) \right\} \end{aligned} \quad (3)$$

where  $\phi_n$  and  $\phi_t$  respectively denote the normal and tangential work of separation, which are given by

$$\phi_n = \exp(1)\sigma_{max}\delta_n \quad (4)$$

$$\phi_t = \sqrt{\frac{\exp(1)}{2}}\tau_{max,0}\delta_t \quad (5)$$

Here,  $\sigma_{max}$  and  $\tau_{max}$  indicate, respectively, the interface normal and tangential strengths, while  $\delta_n$  and  $\delta_t$  refer to the characteristic opening lengths for normal and tangential directions, respectively. The coupling between the latter is governed by  $q = \phi_t/\phi_n$  and  $r = \Delta_n^*/\delta_n$ , where  $\Delta_n^*$  is the value attained by the normal displacement jump after complete shear separation when  $T_n = 0$ . Accordingly, the expressions for the normal,

$$T_n = \frac{\phi_n}{\delta_n} \exp\left(-\frac{\Delta_n}{\delta_n}\right) \left\{ \frac{\Delta_n}{\delta_n} \exp\left(-\frac{\Delta_t^2}{\delta_t^2}\right) + \frac{1-q}{r-1} \left[1 - \exp\left(-\frac{\Delta_t^2}{\delta_t^2}\right)\right] \left[r - \frac{\Delta_n}{\delta_n}\right] \right\} \quad (6)$$

and tangential tractions,

$$T_t = 2\frac{\phi_n}{\delta_t} \frac{\Delta_t}{\delta_t} \left\{ q + \left(\frac{r-q}{r-1}\right) \frac{\Delta_n}{\delta_n} \right\} \exp\left(-\frac{\Delta_n}{\delta_n}\right) \exp\left(-\frac{\Delta_t^2}{\delta_t^2}\right) \quad (7)$$

are readily obtained. Consequently, the cohesive response in the normal direction is shown in Fig. 1. As a rule of thumb, since  $T_n$  is never equal to zero, it is generally assumed that the element has cracked completely when  $\Delta_n = 5\delta_n$ .

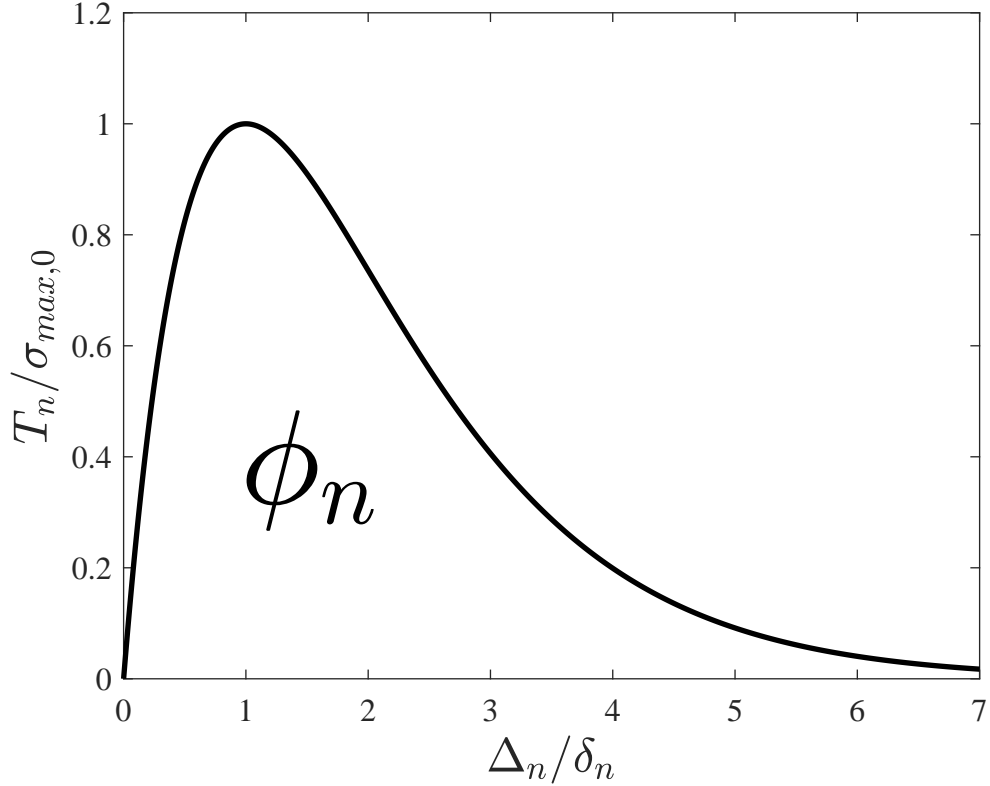


Figure 1: Traction-separation law characterizing Xu and Needleman (1993) cohesive zone model.

## 2.2. Cyclic damage

Focus has been placed on pure mode I fatigue problems and consequently, the constitutive equations related to the tangential separation are omitted for the sake of brevity. Cyclic damage is incorporated by means of the irreversible cohesive zone model proposed by Roe and Siegmund (2003). The model incorporates (i) loading-unloading conditions, (ii) accumulation of damage during subcritical cyclic loading, and (iii) crack surface contact. A damage mechanics approach is adopted to capture the cohesive properties degradation as a function of the number of cycles. A damage variable  $D$  is defined so that it represents the effective surface density of micro defects in the interface. Consequently, an effective cohesive zone traction can be formulated:  $\tilde{\mathbf{T}} = \mathbf{T}/(1 - D)$ . Subsequently, the current or effective cohesive strength

$\sigma_{max}$  is related to the initial cohesive strength  $\sigma_{max,0}$  as,

$$\sigma_{max} = \sigma_{max,0}(1 - D) \quad (8)$$

A 0 is added to the subscript of the critical cohesive traction to emphasize that  $\sigma_{max,0}$  denotes the *initial* normal strengths, as  $\sigma_{max}$  can be reduced due to, e.g., fatigue damage and/or hydrogen embrittlement (see del Busto et al., 2017). A damage evolution law is defined so that it incorporates the relevant features of continuum damage approaches, namely: (i) damage accumulation starts if a deformation measure is greater than a critical magnitude, (ii) the increment of damage is related to the increment of deformation, and (iii) an endurance limit exists, below which cyclic loading can proceed infinitely without failure. From these considerations, cyclic damage evolution is defined as,

$$\dot{D}_c = \frac{|\dot{\Delta}_n|}{\delta_\Sigma} \left[ \frac{T_n}{\sigma_{max}} - \frac{\sigma_f}{\sigma_{max,0}} \right] H(\bar{\Delta}_n - \delta_n) \quad (9)$$

with  $\bar{\Delta}_n = \int |\dot{\Delta}_n| dt$  and  $H$  denoting the Heaviside function. Two new parameters have been introduced:  $\sigma_f$ , the cohesive endurance limit and  $\delta_\Sigma$ , the accumulated cohesive length - used to scale the normalized increment of the effective material separation. The modeling framework must also incorporate damage due to monotonic loading; as a consequence, the damage state is defined as the maximum of the cyclic and monotonic contributions,

$$D = \int \max(\dot{D}_c, \dot{D}_m) dt \quad (10)$$

being the latter characterized as:

$$\dot{D}_m = \frac{\max(\Delta_n)|_{t_i} - \max(\Delta_n)|_{t_{i-1}}}{4\delta_n} \quad (11)$$

and updated only when the largest stored value of  $\Delta_n$  is greater than  $\delta_N$ . Here,  $t_{i-1}$  denotes the previous time increment and  $t_i$  the current one. In addition to damage evolution, the cohesive response must be defined for the cases of unloading/reloading, compression, and contact between the crack faces. Unloading is defined based on the analogy with an elastic-plastic material undergoing damage. Thereby, unloading takes place with the stiffness of the cohesive zone at zero separation, such that

$$T_n = T_{max} + \left( \frac{\exp(1)\sigma_{max}}{\delta_n} \right) (\Delta_n - \Delta_{max}) \quad (12)$$

where  $\Delta_{max}$  is the maximum separation value that has been attained and  $T_{max}$  its associated traction quantity. Compression behavior applies when the unloading path reaches  $\Delta_n = 0$  at  $T_n < 0$ . In such circumstances, the cohesive response is given by,

$$T_n = \frac{\phi_n}{\delta_n} \left( \frac{\Delta_n}{\delta_n} \right) \exp \left( -\frac{\Delta_n}{\delta_n} \right) + T_{max} - \sigma_{max} \exp(1) \frac{\Delta_{max}}{\delta_n} + \alpha \sigma_{max,0} \exp(1) \frac{\Delta_n}{\delta_n} \exp \left( -\frac{\Delta_n}{\delta_n} \right) \quad (13)$$

being  $\alpha$  a penalty factor that is taken to be equal to 10, following (Roe and Siegmund, 2003). Contact conditions are enforced if  $\Delta_n$  is negative and the cohesive element has failed completely ( $D = 1$ ). At this instance the cohesive law renders,

$$T_n = \alpha \sigma_{max,0} \exp(1) \exp \left( -\frac{\Delta_n}{\delta_n} \right) \frac{\Delta_n}{\delta_n} \quad (14)$$

where friction effects have been neglected. Fig. 2 shows a representative response obtained by applying a stress-controlled cyclic loading  $\Delta\sigma/\sigma_{max,0} = 1$  with a zero stress ratio. The accumulated separation increases with the number of loading cycles, so that it becomes larger than  $\delta_n$  and damage starts to play a role, lowering the stiffness and the cohesive strength.

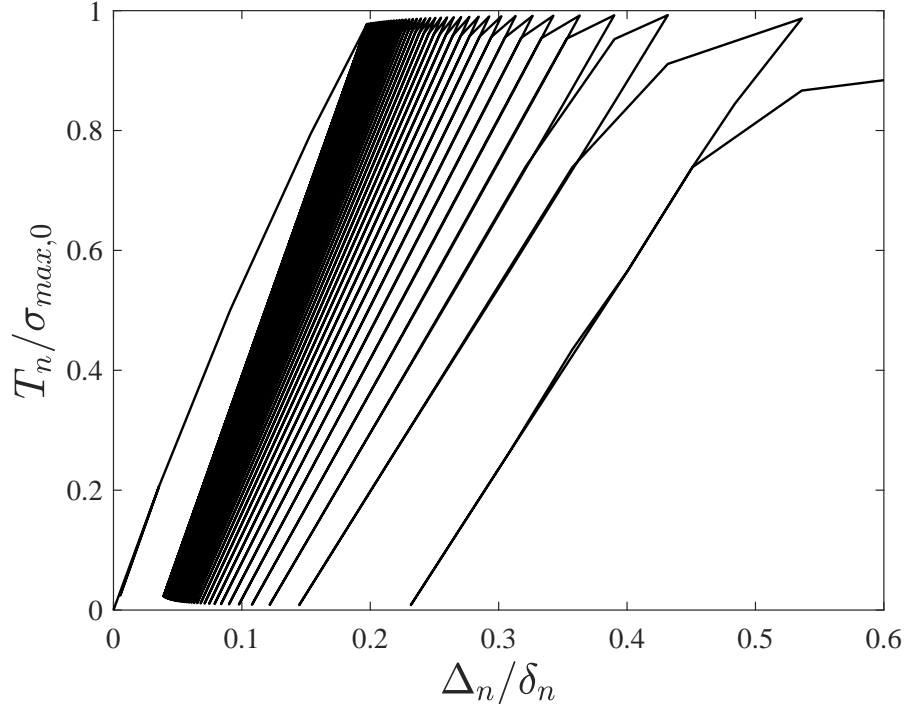


Figure 2: Cohesive response under stress-controlled cyclic loading conditions.

### 3. Finite element implementation

Damage is restricted to evolve along the predefined cohesive interface, and consequently, the numerical implementation is generally conducted by inserting cohesive finite elements in potential crack propagation paths. Hence, in the absence of body forces, the weak form of the equilibrium equations for a body of volume  $V$  and external surface  $S$  renders,

$$\int_V \boldsymbol{\sigma} : \delta \boldsymbol{\varepsilon} dV + \int_{S_c} \mathbf{T} \cdot \delta \boldsymbol{\Delta} dS = \int_S \mathbf{t} \cdot \delta \mathbf{u} dS \quad (15)$$

Here,  $\mathbf{T}$  are the cohesive tractions and  $S_c$  is the surface across which these tractions operate. The standard part of the mechanical equilibrium statement is characterized by the Cauchy stress tensor  $\boldsymbol{\sigma}$ , the work-conjugate strain tensor  $\boldsymbol{\varepsilon}$ , the external tractions  $\mathbf{t}$  and the displacement vector  $\mathbf{u}$ ; the latter being obtained by interpolating the global nodal displacement  $\mathbf{u} =$

**NU.** We focus here on the most general case: large strains and rotations, including both normal and tangential separations (mixed mode). Such that, for (e.g.) a 4-node cohesive element, the nodal global displacements are given by,

$$\mathbf{U} = \left( \tilde{U}_1, \tilde{U}_2, \tilde{U}_3, \tilde{U}_4, \tilde{U}_5, \tilde{U}_6, \tilde{U}_7, \tilde{U}_8 \right) \quad (16)$$

If large rotations occur we should change our global coordinate system to a local coordinate system, where the local Lagrangian coordinate system rotates with the element, as outlined in the figure below.

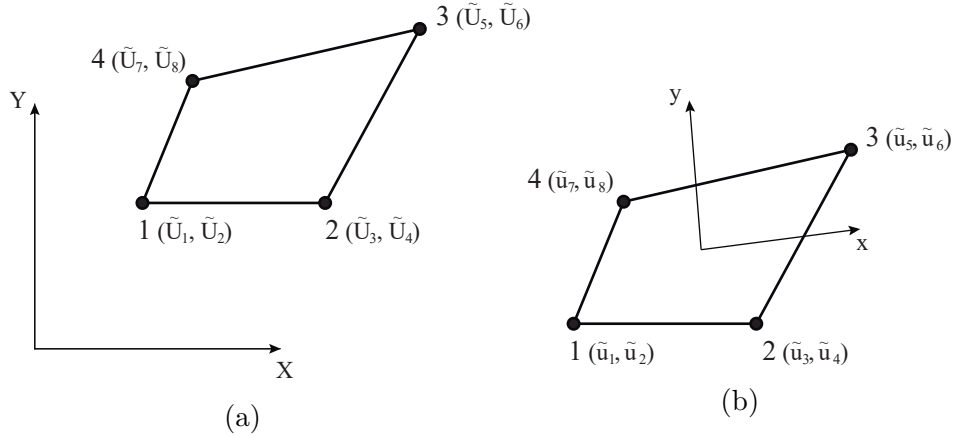


Figure 3: Nodal displacements in (a) global and (b) local coordinate systems.

In such scheme, the local nodal displacements are given by:

$$\tilde{\mathbf{u}}_i = (\tilde{u}_1, \tilde{u}_2, \tilde{u}_3, \tilde{u}_4, \tilde{u}_5, \tilde{u}_6, \tilde{u}_7, \tilde{u}_8) \quad (17)$$

The local axis is identified by computing the midside points of the element, with the tangential axis ( $x$ ) being the line connecting those midside points, as outlined below.

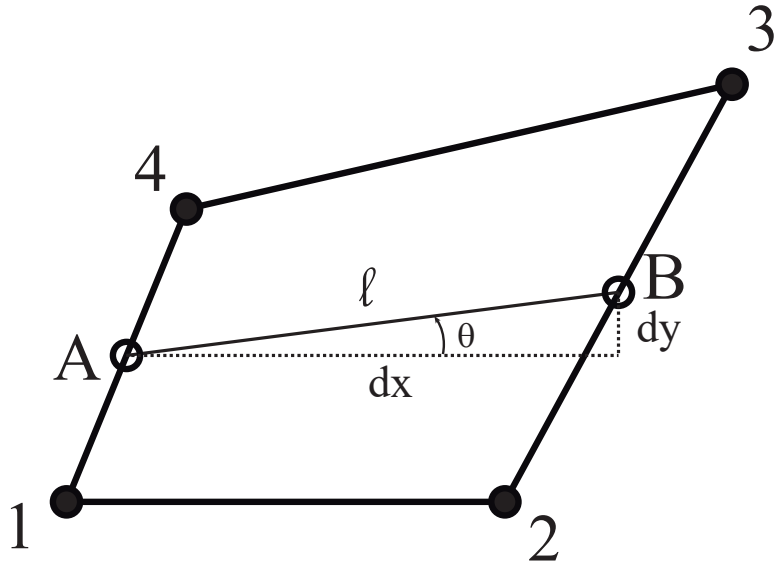


Figure 4: Midpoints and local axis

A rotational matrix is employed to change between the local and global displacements. Thus, the local  $\xi$  and global  $\Xi$  coordinates are related,

$$\xi = \Upsilon \Xi \quad (18)$$

through  $\Upsilon$ , a coordinate transformation matrix: (see Fig. 4)

$$\Upsilon = \begin{bmatrix} \cos \theta & \sin \theta \\ -\sin \theta & \cos \theta \end{bmatrix} \quad (19)$$

and accordingly, local and global displacements are related through the rotational matrix,

$$\tilde{u} = \mathbf{R}u \quad (20)$$

that, for a 4-node cohesive element, equals:

$$\mathbf{R} = \begin{bmatrix} \Upsilon & 0 & 0 & 0 \\ 0 & \Upsilon & 0 & 0 \\ 0 & 0 & \Upsilon & 0 \\ 0 & 0 & 0 & \Upsilon \end{bmatrix} \quad (21)$$

The procedure is therefore as follows:

(i) Computation the nodal coordinates in the deformed configuration  $(x_i, y_i)$  from the nodal coordinates in the undeformed configuration  $(X_i, Y_i)$  and the global nodal displacements  $(\tilde{U}_i)$ :

$$(x_1, y_1) = (X_1 + \tilde{U}_1, Y_1 + \tilde{U}_2) \quad (22)$$

$$(x_2, y_2) = (X_2 + \tilde{U}_3, Y_2 + \tilde{U}_4) \quad (23)$$

$$(x_3, y_3) = (X_3 + \tilde{U}_5, Y_3 + \tilde{U}_6) \quad (24)$$

$$(x_4, y_4) = (X_4 + \tilde{U}_7, Y_4 + \tilde{U}_8) \quad (25)$$

(ii) Computation of the mid-point coordinates:

$$(x_A, y_A) = \frac{1}{2}(x_1 + x_4, y_1 + y_4) \quad (26)$$

$$(x_B, y_B) = \frac{1}{2}(x_2 + x_3, y_2 + y_3) \quad (27)$$

(iii) Computation the horizontal and vertical length of the mid segment:

$$dx = x_B - x_A \quad (28)$$

$$dy = y_B - y_A \quad (29)$$

(iv) Computation of the cohesive element length:

$$\ell = \sqrt{dx^2 + dy^2} \quad (30)$$

(v) Computation of the components of the rotational matrix through trigonometric relations:

$$\cos \theta = \frac{dx}{\ell} \quad (31)$$

$$\sin \theta = \frac{dy}{\ell} \quad (32)$$

One can now compute the local nodal displacements  $\tilde{\mathbf{u}}$  through (20). The local separation  $\tilde{\Delta}$  is related to  $\tilde{\mathbf{u}}$  by means of a local displacement-separation relation matrix  $\mathbf{L}$ ,

$$\tilde{\Delta} = \mathbf{L}\tilde{\mathbf{u}} \quad (33)$$

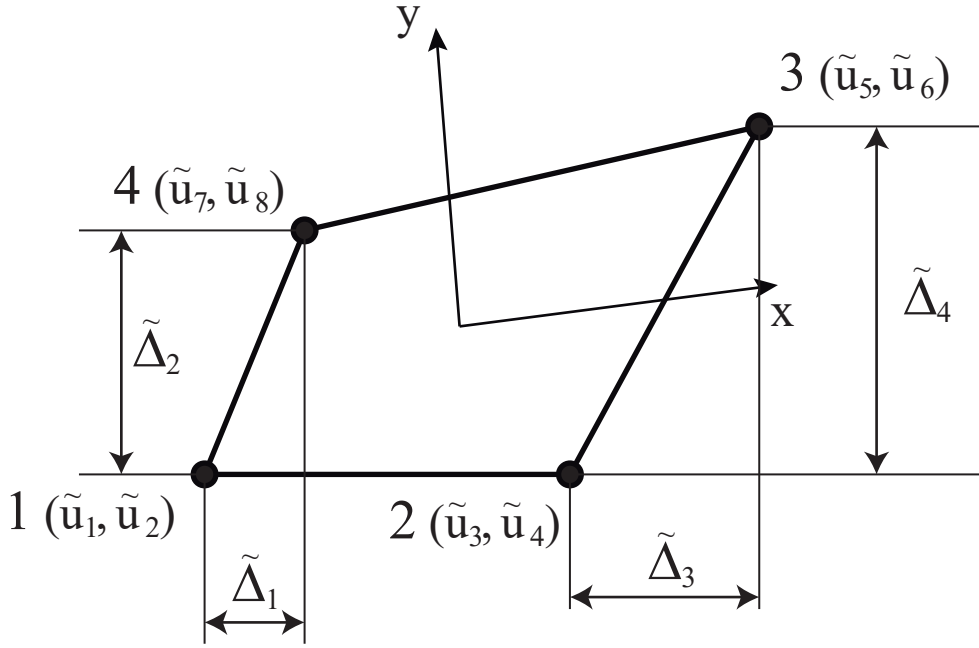


Figure 5: Local separation

For the case of the 4-node element that is being considered, the components of  $\mathbf{L}$  can be easily determined by the existing relation between normal and tangential components of the local separation at the mid-points and the local nodal displacements (see Fig. 5),

$$\tilde{\Delta}_1 = \tilde{u}_7 - \tilde{u}_1 \quad (34)$$

$$\tilde{\Delta}_2 = \tilde{u}_8 - \tilde{u}_2 \quad (35)$$

$$\tilde{\Delta}_3 = \tilde{u}_5 - \tilde{u}_3 \quad (36)$$

$$\tilde{\Delta}_4 = \tilde{u}_6 - \tilde{u}_4 \quad (37)$$

implying that,

$$\mathbf{L} = \begin{bmatrix} -1 & 0 & 0 & 0 & 0 & 0 & 1 & 0 \\ 0 & -1 & 0 & 0 & 0 & 0 & 0 & 1 \\ 0 & 0 & -1 & 0 & 1 & 0 & 0 & 0 \\ 0 & 0 & 0 & -1 & 0 & 1 & 0 & 0 \end{bmatrix} \quad (38)$$

The local normal and tangential separation at the mid-points are interpolated through the element as we rely on numerical integration to solve the cohesive element constitutive matrix. The separation along a cohesive surface element is interpolated from the nodal separation by means of standard shape functions,

$$\Delta = \mathbf{N}\tilde{\Delta} \quad (39)$$

The relationship between the local separation and the global nodal displacement can be then obtained by combining the previous equations,

$$\Delta = \mathbf{B}_c \mathbf{U} \quad (40)$$

where  $\mathbf{B}_c$  is a global displacement-separation relation matrix:  $\mathbf{B}_c = \mathbf{N}\mathbf{L}\mathbf{R}$ . Thus, accounting for the classic finite element discretization in (15) and requiring the variational statement to hold for any admissible field, it renders

$$\int_V \mathbf{B}^T \mathcal{L} \boldsymbol{\varepsilon} dV + \int_{S_c} \mathbf{B}_c^T \mathbf{T} dS = \int_S \mathbf{N}^T \mathbf{t} dS \quad (41)$$

where  $\mathcal{L}$  is the elastoplastic constitutive matrix and  $\mathbf{B}$  the standard strain-displacement matrix. Considering the dependence of  $\boldsymbol{\varepsilon}$  and  $\mathbf{T}$  on  $\mathbf{U}$ ,

$$\mathbf{U} \left( \int_V \mathbf{B}^T \mathcal{L} \mathbf{B} dV + \int_{S_c} \mathbf{B}_c^T \frac{\partial \mathbf{T}}{\partial \Delta} \mathbf{B}_c dS \right) = \int_S \mathbf{N}^T \mathbf{t} dS \quad (42)$$

and the components of the classic finite element global system of equations can be readily identified. The stiffness matrix of the cohesive elements is therefore given by,

$$\mathbf{K}_c = \int_{S_c} \mathbf{B}_c^T \frac{\partial \mathbf{T}}{\partial \Delta} \mathbf{B}_c dS \quad (43)$$

which corresponds to the gradient of the internal cohesive force vector,

$$\mathbf{f}_c = \int_{S_0} \mathbf{B}_c^T \mathbf{T} dS \quad (44)$$

## 4. Usage instructions

We now particularize the previously described numerical implementation by focusing on the specific setup of the attached code: 2D problems, Mode-I symmetric models and quadratic cohesive elements. The use of quadratic cohesive elements is particularly convenient to reduce computational time, and it is necessary when dealing with non-local theories of plasticity (Martínez-Pañeda and Betegón, 2015; Martínez-Pañeda and Niordson, 2016) or hydrogen assisted cracking (del Busto et al., 2017; Martínez-Pañeda et al., 2016). Moreover, we take advantage of adopt what is sometimes referred to a *cohesive forces* scheme, favored by Needleman and co-workers, so as to avoid defining new degrees of freedom - no new elements are defined and the cohesive contributions relate to the conventional nodes ahead of the crack tip. Some comments regarding the specific framework provided follow.

### 4.1. Mode I and symmetric models

Mode I fracture is the most pernicious mode of cracking and has therefore attracted a great deal of attention from academics and practitioners. Under such circumstances only the normal terms of the cohesive traction are non-zero.

Moreover, it is quite common to take advantage of symmetry conditions to model cracking in the specimen under consideration. In such circumstances, a frequent procedure is to constraint the vertical displacement of the bottom nodes of the cohesive element, as depicted in Fig. 6.

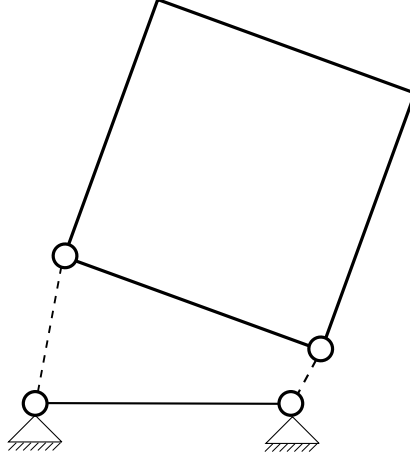


Figure 6: Cohesive element in a symmetric configuration.

However, one should note that if a cohesive element is placed at a line of symmetry, it will undergo an unsymmetric deformation if simply the displacements of the bottom nodes are constrained. The midsegment will rotate and the horizontal displacement of the bottom and top nodes will be different, resulting in shear separation  $\Delta_t$ . This can be prevented by using the coordinate system of the undeformed configuration and imposing  $\Delta_t = 0$  (a flag variable has been defined in the present code). It is important to note as well that in a symmetric model the cohesive energy to overcome is half of the cohesive energy of the full model. Or, in other words, the contribution of the cohesive element is divided by two, i.e.

$$\int_V \boldsymbol{\sigma} : \delta \boldsymbol{\varepsilon} \, dV + \frac{1}{2} \int_{S_c} \mathbf{T} \cdot \delta \boldsymbol{\Delta} \, dS = \int_S \mathbf{t} \cdot \delta \mathbf{u} \, dS \quad (45)$$

A simple way of proceeding relies in keeping the same value of the maximum cohesive stress but making half the magnitude of the critical separation parameter(s).

As it can be readily inferred from Fig. 6, if the response is symmetric the model can be further simplified by avoiding to define additional DOFs; the displacement of the nodes at the top suffices to compute the local separation.

#### 4.2. Convergence problems

Cohesive zone models may suffer of convergence problems due to the occurrence of an elastic snap-back instability. In order to facilitate numerical

convergence the present code includes the viscous regularization technique proposed by Gao and Bower Gao and Bower (2004). Such scheme leads to accurate results if the viscosity coefficient,  $\xi$ , is sufficiently small. A sensitivity study must be conducted in all cases where viscous regularization is needed. As described in (Gao and Bower, 2004), a small additional viscous dissipation is added to the traction-separation relation,

$$T_n = \frac{\phi_n}{\delta_n} \exp\left(-\frac{\Delta_n}{\delta_n}\right) \left\{ \frac{\Delta_n}{\delta_n} \exp\left(-\frac{\Delta_t^2}{\delta_t^2}\right) + \frac{1-q}{r-1} \left[1 - \exp\left(-\frac{\Delta_t^2}{\delta_t^2}\right)\right] \left[r - \frac{\Delta_n}{\delta_n}\right] \right\} + \xi \frac{d}{dt} \left(\frac{\Delta_n}{\delta_n}\right) \quad (46)$$

where  $\xi$  is the viscosity-like parameter, which has no physical meaning and is only used to regularize instabilities. Making  $\xi = 0$  suppresses the viscosity contribution.

#### 4.3. Abaqus peculiarities and example

A very simple example is provided to ease the use of the subroutine. Hence, a square plate of dimensions 0.1 x 0.1 mm is subjected to uniaxial loading in the vertical direction by prescribing the displacement of the nodes in the upper edge. The specimen is modeled by means of only one continuum quadratic plane stress element with 8 nodes and 4 integration points. Linear elastic behavior is assumed in the bulk, with Young's modulus  $E = 200$  GPa and Poisson's ratio  $\nu = 0.3$ . The traction-separation response is given by (Xu and Needleman, 1993) cohesive law, with  $\sigma_{max,0} = 600$  MPa and  $\delta_n = 0.0002$  mm. We adopt the *cohesive forces* approach, and consequently no additional degrees of freedom are defined. Thus, the cohesive element has three nodes (as denoted in Fig. 7) and 12 integration points. The number of integration points can be defined in the input file by the user. One should however note that our numerical tests clearly indicate that using 12 integration points is certainly beneficial in terms of convergence and computational cost. The use of cohesive zone models requires a very refined mesh ahead of the crack, and a mesh sensitivity study is therefore essential.

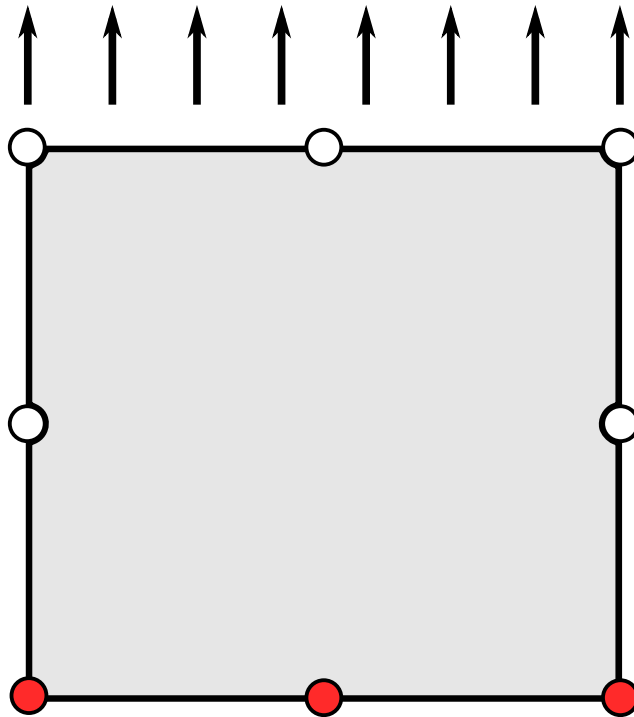


Figure 7: Configuration of the 1-element example. Cohesive nodes are marked in red.

The cohesive element is defined in the input file by means of the following lines,

```
*USER ELEMENT, TYPE=U1, NODES=3, COORDINATES=2, PROPERTIES=9, VARIABLES=60
1,2
*ELEMENT, TYPE=U1, ELSET=ONE
2, 1, 5, 2
*UEL PROPERTY, ELSET=ONE
600., 0.0002, 0.0002, 1, 0, 1, 0.25, 12, 0.
```

In that way, the vast majority of the variables of the analysis are defined without modifying the Fortran code. As seen above, 9 user-defined properties are employed in the UEL subroutine; they are described in Table 1.

Table 1: Equivalence between the properties and the corresponding variables.

PROPS	Variable
1	$\sigma_{max,0}$ - Initial cohesive strength in the normal direction
2	$\delta_n$ - Characteristic cohesive length in the normal direction
3	$\delta_t$ - Characteristic cohesive length in the tangential direction
4	$q$ - Coupling parameter in Xu and Needleman (1993) law
5	$r$ - Coupling parameter in Xu and Needleman (1993) law
6	Flag variable
7	$C_f = \sigma_f / \sigma_{max,0}$ - Endurance coefficient
8	Number of integration points (it can be 3, 6 or 12)
9	$\xi$ - Viscosity coefficient

The flag variable should be assigned the value 0 when modeling the entire specimen under the finite strain assumption, the value 1 when taking advantage of symmetry in a small strains problem and the value of 2 if we have symmetric conditions and large deformations. In addition, 5 solution-dependent state variables (SVARS) are defined per integration point to store information that must be transferred between increments (12 integration points, a total of 80 SVARS). Table 2 shows the specific allocation of these set of 5 variables at each integration point.

Table 2: Equivalence between the SVARS in the UEL and the corresponding variables.

SVARS	Variable
1	$D$ - Damage variable
2	$\Delta_{max}$ - Maximum separation value that has been attained
3	$T_{max}$ - Traction associated with $\Delta_{max}$
4	$ \Delta_n _{t_{i-1}}$ - Normal separation in the previous increment
5	Largest stored value of $\Delta_n$

The input file of the simple benchmark example provided is also included with the code. To run the calculation type in the command line:

```
abaqus job=Job-1 user=UEL3.f
```

where Job-1 is the name of the input file (Job-1.inp). Depending on the Fortran compiler version, some Windows users may have to use the UEL3.for file instead, such that the command line would look like,

```
abaqus job=Job-1 user=UEL3.for
```

The results obtained by prescribing a remote displacement of 0.001 mm are shown in Fig. 8. Results show the opening stress versus the separation of the crack face. The figure can be easily obtained by creating XY Data from the History Output information; namely, the stress in the vertical direction and the displacement of the node in the lower left corner. A python script is also provided to obtain the results - other options include the use of *Abaqus2Matlab*, a novel tool to postprocess Abaqus' results in Matlab (see Papazafeiropoulos et al., 2017).

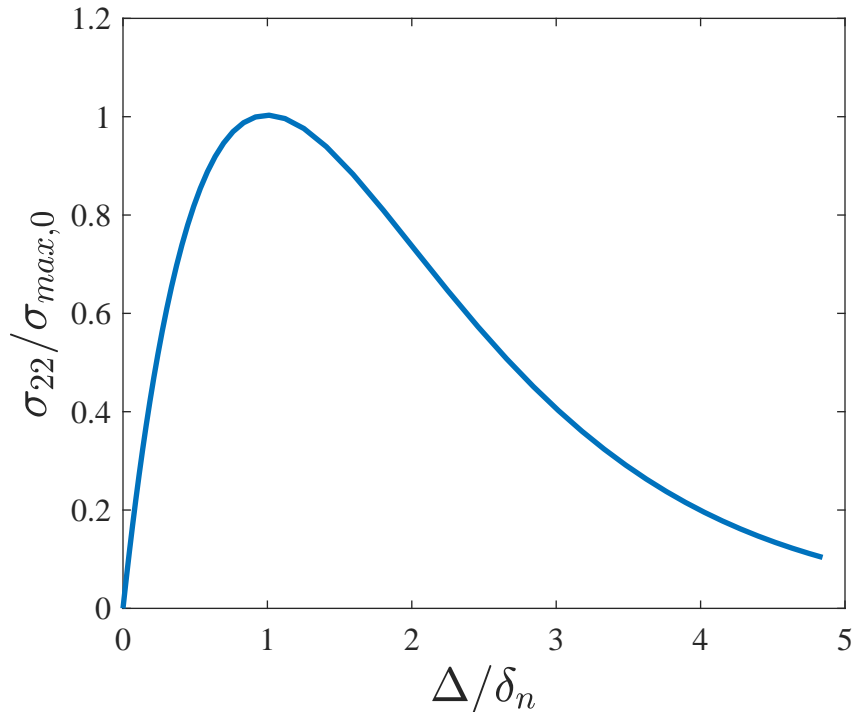


Figure 8: Stress versus separation response predicted in the simple 1-element example.

As it can be easily observed, the opening stresses in the bulk increase until

a critical point is reached, at which the opening stress equals the cohesive strength and  $\Delta_n = \delta_n$ . Damage then initiates and softening takes place.

#### 4.4. Limitations

The present cohesive zone model can be easily extended to: (i) mixed-mode problems, (ii) three dimensions, (iii) other traction-separation relations, and (iv) accounting for hydrogen degradation, among many other possibilities. Some of these extensions have already been conducted and the associated part of the code can be provided on request.

## 5. Conclusions

If the code and the documentation provided here are useful please cite:

S. del Busto, C. Betegón, E. Martínez-Pañeda. A cohesive zone framework for environmentally assisted fatigue. *Engineering Fracture Mechanics* 185, pp. 210-226 (2017)

Do not hesitate to contact for further clarifications.

## 6. Acknowledgments

E. Martínez-Pañeda acknowledges financial support from the People Programme (Marie Curie Actions) of the European Union's Seventh Framework Programme (FP7/2007-2013) under REA grant agreement n° 609405 (CO-FUNDPstdocDTU).

## References

- del Busto, S., Betegón, C., Martínez-Pañeda, E., 2017. A cohesive zone framework for environmentally assisted fatigue. *Engineering Fracture Mechanics* 185, 210–226.
- Gao, Y. F., Bower, A. F., 2004. A simple technique for avoiding convergence problems in finite element simulations of crack nucleation and growth on cohesive interfaces. *Modelling and Simulation in Materials Science and Engineering* 12 (3), 453–463.
- Kuna, M., 2013. *Finite Elements in Fracture Mechanics*. Vol. 201. Springer.

- Martínez-Pañeda, E., Betegón, C., 2015. Modeling damage and fracture within strain-gradient plasticity. *International Journal of Solids and Structures* 59, 208–215.
- Martínez-Pañeda, E., Niordson, C. F., 2016. On fracture in finite strain gradient plasticity. *International Journal of Plasticity* 80, 154–167.
- Martínez-Pañeda, E., Niordson, C. F., Gangloff, R. P., 2016. Strain gradient plasticity-based modeling of hydrogen environment assisted cracking. *Acta Materialia* 117, 321–332.
- McGarry, J. P., Ó Máirtín, É., Parry, G., Beltz, G. E., 2014. Potential-based and non-potential-based cohesive zone formulations under mixed-mode separation and over-closure. Part I: Theoretical analysis. *Journal of the Mechanics and Physics of Solids* 63 (1), 336–362.
- Papazafeiropoulos, G., Muñiz-Calvente, M., Martínez-Pañeda, E., 2017. Abaqus2Matlab: A suitable tool for finite element post-processing. *Advances in Engineering Software* 105, 9–16.
- Park, K., Paulino, G. H., 2013. Cohesive Zone Models: A Critical Review of Traction-Separation Relationships Across Fracture Surfaces. *Applied Mechanics Reviews* 64 (6), 060802.
- Roe, K., Siegmund, T., 2003. An irreversible cohesive zone model for interface fatigue crack growth simulation. *Engineering Fracture Mechanics* 70 (2), 209–232.
- Xu, X. P., Needleman, A., 1993. Void nucleation by inclusion debonding in a crystal matrix. *Modelling and Simulation in Materials Science and Engineering* 1 (2), 111–132.